Electronic Supplementary Material (ESI) for Physical Chemistry Chemical Physics.

Supporting Information

Mitigating Mechanical Failure of Crystalline Silicon Electrodes for Lithium Batteries by Morphological Design

Yonghao An[a,b,c], Brandon C. Wood[b], Jianchao Ye[b], Yet-Ming Chiang[c], Yinmin Morris Wang[b], Ming Tang[*d], Hanqing Jiang[*a]

[a]School for Engineering of Matter, Transport and Energy, Arizona State University, Tempe, AZ 85286, USA

[b]Physical and Life Science Directorate, Lawrence Livermore National Laboratory, Livermore, CA 94550, USA

[c]Department of Materials Science and Engineering, Massachusetts Institute of Technology, MA 02139, USA

[d]Department of Materials Science and NanoEngineering, Rice University, Houston, TX 77024, USA

*Contact Emails: mingtang@rice.edu, Hanqing.Jiang@asu.edu

Additional Details of Simulation Method

In numerical simulations of the lithiation process, the loci of ACI are updated by a front tracking method. As illustrated in Figure S1, the ACI, which is a curve for 2D pillar simulations and surface for 3D particle simulations, is discretized by a set of points with equal separation. A sufficient number of points, typically 360 points for 2D and 64800 points for 3D simulations, are used to ensure the convergence of simulations. The tangential lines or planes at these points are determined. For each time step Δt, the tangent lines or planes are moved inwards along their normals by a distance $v(\boldsymbol{n})\Delta t$, where $v(\boldsymbol{n})$ is the orientation-dependent interface velocity evaluated by Equation 4 in the main text, and the new positions of ACI are determined by the

envelope of the updated tangent lines or planes. Following the update of ACI positions, the Li concentration field is also updated by assigning $\overline{c}$ =0 inside ACI and $\overline{c}$ =1 outside ACI. In addition, a smooth variation of $\overline{c}$ between 0 and 1 is imposed within a very thin layer across ACI to facilitate numerical convergence. The algorithm described above is implemented in ABAQUS user subroutine UTEMP. Another user subroutine UEXPAN is employed to specify the stress-free strain of *a*-Li_xSi resulting from lithiation-induced volume expansion in a way consistent with the total Lagrangian description for large deformation (see detailed discussion is our previous work[1]). The mechanical constitution is implemented by ABAQUS build-in modules for concentration-dependent properties, using the implicit plastic-elastic solver with the nonlinear geometry option turned on for large deformation problems.

Additional Details of Experimental Method

Micropillars on (100) Si wafers were defined photolithographically with masks in circle and square shapes. The latter has edge orientations along {110} planes. The diameter, spacing, and height of the micropillars are 2 μm, 2 μm, and 50 μm, respectively. The micropillars were etched out by a Bosch process[2] during which the isotropic etching step using 25 sccm SF_6 plasma and the passivizing polymerization step using 80 sccm C_4F_8 were alternated repeatedly until the desired height was achieved.

Swagelok-type half-cells were assembled in Argon-filled glove box with oxygen and water content less than 1 ppm for electrochemical lithiation. 1M LiPF6 in mixed ethylene carbonate (EC)/ diethyl carbonate (DEC)/ dimethyl carbonate (DMC) (1:1:1 in volume) was used as the electrolyte. Two layers of polypropylene microporous films (Celgard 3501) were used as

the separator. Si micropillars on wafer chip were directly assembled into the cell as the working electrode and lithium chip with thickness of 250 μm and diameter of 9 mm was adopted as the counter electrode. Partial lithiation was carried out in a Maccor 4304 battery cycler. The circular p-type micropillars shown in Figure 6(a) was lithiated at constant current density of 11 mA/cm^2 for 2000 s. The square p-type micropillars shown in Figure 6(d) was lithiated by scanning the cell voltage from the open circuit potential (~3V vs Li/Li$^+$) to 50 mV at a constant scan rate of 0.1 mV/s and then held at 50 mV for 20 hours. Afterwards the micropillar samples were washed with DMC, dried in a glove box and sealed in Ar-filled glass vials to be taken out for scanning electron microscopy (SEM) characterizations. SEM analysis was performed on a JOEL 7401-F system with an accelerating voltage of 2 kV and a working distance of ~6 mm.

Evaluation of the Anisotropy Parameter η

In the main text, the parameter η is used to describe the relative lithiation velocity along <100> with respect to <110>. A η value of 1/6 is used in simulation and the ordering of interface velocities in three main directions is set as: $v_{<111>} < v_{<100>} < v_{<110>}$. As a motivation for our choice of η and this ordering, we performed density functional theory (DFT) calculations of strain energy for thin surface slabs aligned along each of these directions. Each of the slabs was eight layers thick and carved from the corresponding bulk geometry. Surface reconstruction and atomic relaxation are not considered in the calculations, since there is no evidence that reconstruction will occur at the reaction front with lithiated *a*-Si, where ion mobility and entropy are high, and ions are freely available to passivate dangling bonds and equilibrate local potentials. The system therefore simulates two surface-vacuum interfaces with four independent layers each; the thin slabs were deliberately chosen so as to ensure that the calculated strain energies are

associated with surface rather than bulk character. To compute the strain energies, biaxial strain was applied within the surface plane only.

Periodic boundary conditions were applied, with 12 Å vacuum inserted perpendicular to the slab direction. An ultrasoft pseudopotential[3] with the Perdew-Burke-Ernzerhof (PBE) exchange-correlation functional[4] was employed for Si, with plane wave and charge density cutoffs of 24 Ry and 240 Ry, respectively, as implemented in the Quantum ESPRESSO code[5]. A Monkhorst-Pack[6] **k**-point mesh was used, based on a primitive-cell sampling of (6×6×6) and scaled appropriate to the surface of interest.

The Li insertion barrier is expected to correlate with the strain energy associated with locally expanding the slab parallel to the surface, so as to accommodate the diffusing Li. However, because the surface boundary conditions are fixed by the underlying crystalline Si lattice immediately beyond the amorphous-crystalline interface, we assume that local expansion must be accompanied by secondary local lattice compression, such that the total area of the surface is conserved. Accordingly, we examine the surface slabs under both tensile and compressive strain.

The area-specific strain energy for the slabs is shown as a function of strain in Figure S7(a). Note that the strain is defined relative to the equilibrium bulk lattice parameter, which does not necessarily correspond to the equilibrium lattice parameter of the surface slab due to intrinsic surface stress. Accordingly, the (100) and (111) surfaces have intrinsic compressive surface stress (minimum strain energy occurs below the bulk equilibrium lattice spacing), whereas the (110) surface has weak intrinsic tensile surface stress. To estimate the total strain energy *s* introduced by straining the lattice to accommodate Li insertion, we average the area-

normalized strain energy induced by tension with the equivalent quantity induced by compression, according to:

$$s = \frac{\Delta E^{+} + \Delta E^{-}}{2A_0}$$

where ΔE^{+} and ΔE^{-} are changes in total internal energy associated with the application of local tensile (+) and compressive (-) strain, and A_0 is the surface area of the slab at the equilibrium bulk lattice parameter. Note that this definition assumes the total surface area of the slab is conserved, as indicated above. As shown in Figure S7(b), the quantity s is smallest for the (110) plane and largest for the (111) plane, with the intermediate (100) result far closer to the (111) value than the (110) value. This means that the relative interface velocities of reaction fronts perpendicular to these planes, which are exponentially dependent on the insertion barriers via an Arrhenius relation, should have the ordering $v_{<110>} >> v_{<100>} > v_{<111>}$. We can use our computed values of s to calculate a composite strain ratio $r = \frac{s_{(111)} - s_{(100)}}{s_{(111)} - s_{(110)}}$, which describes the relative insertion barrier along <100> with respect to <110> and <111> and is related to the choice of the parameter η. For non-negligible strains, the ratio r has an upper bound of ~0.4, but decreases with increasing magnitude of the local surface strain induced upon Li insertion. In the immediate vicinity of Li, it is reasonable to assume that local areal strains greater than 10% may be observed, which lowers the expected value of r to less than 0.2. Considering the exponential dependence of reaction front velocity on reaction energy barrier, we conclude that η must be a small value significant lower than 0.5, which justifies our choice of 1/6. Notably, as we show for one example geometry in Figure S7, our conclusions do not change qualitatively if we set η to be even smaller (i.e., zero).

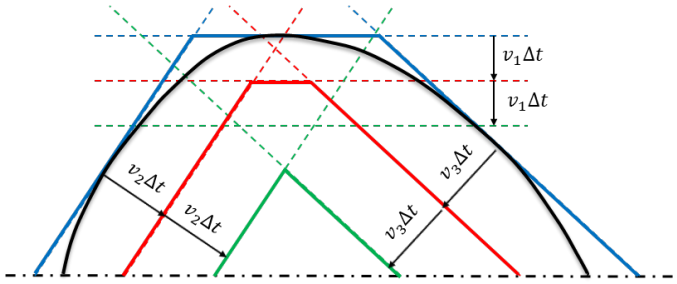

Figure S1. Illustration of how the front tracking method updates ACI positions. Initially, the ACI (black line) is discretized by a set of points with equal separation and their tangent lines form an envelope (blue lines) of ACI. Upon every time step, the tangential lines move inwards by a distance of $v(\mathbf{n})\Delta t$ in their normal directions, and the envelope they form (red and green lines) determines the new positions of ACI.

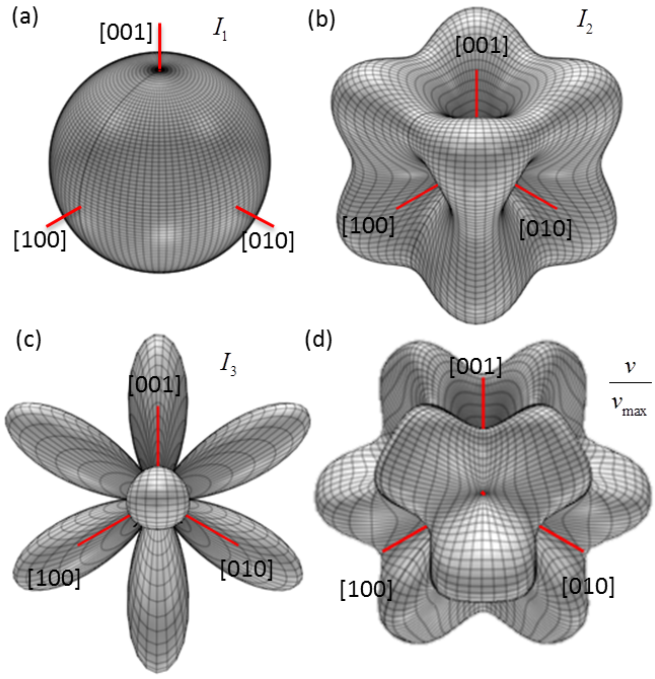

Figure S2. Plots of invariant polynomials (a) $I_1(\mathbf{n})$, (b) $I_2(\mathbf{n})$ and (c) $I_3(\mathbf{n})$ in spherical coordinate. (d) Spherical plot of normalized ACI velocity, $v(\mathbf{n})/v_{max}$, for parameter η=1/6.

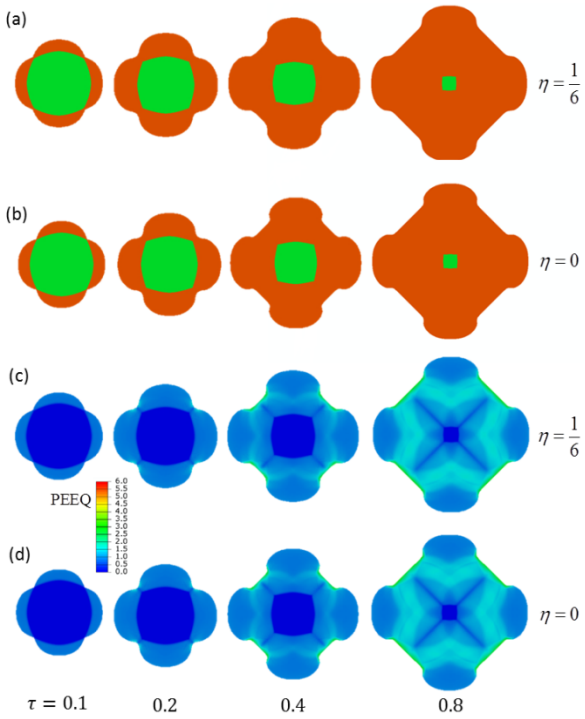

Figure S3. Effect of the value of anisotropy parameter η on simulation results of the lithiation of c-Si pillars. Snapshots of pillar morphology and PEEQ distribution in a <100> pillar at different normalized lithiation times are shown in (a) and (c), respectively for η = 1/6, and (b) and (d) for η = 0. Results for the two values are very similar, confirming the insensitivity of our results to the specific value of η.

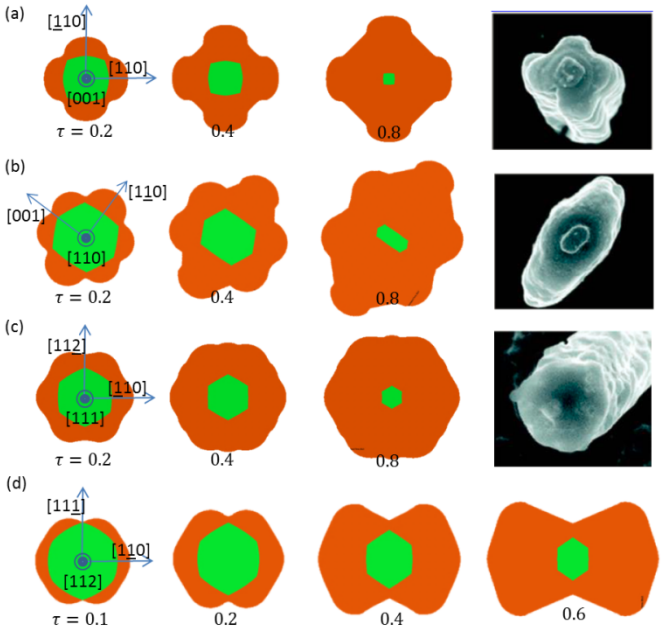

Figure S4. Lithiation simulation of c-Si pillars of four typical axial orientations. Snapshots of the morphology of a-Li_xSi shell (red) and c-Si core (green) at different lithiation times are shown for (a) <100>, (b) <110>, (c) <111> and (d) <112> pillars. SEM images of Si nanopillar morphology from Reference7 are also shown in (a)-(c) for comparison with simulation.

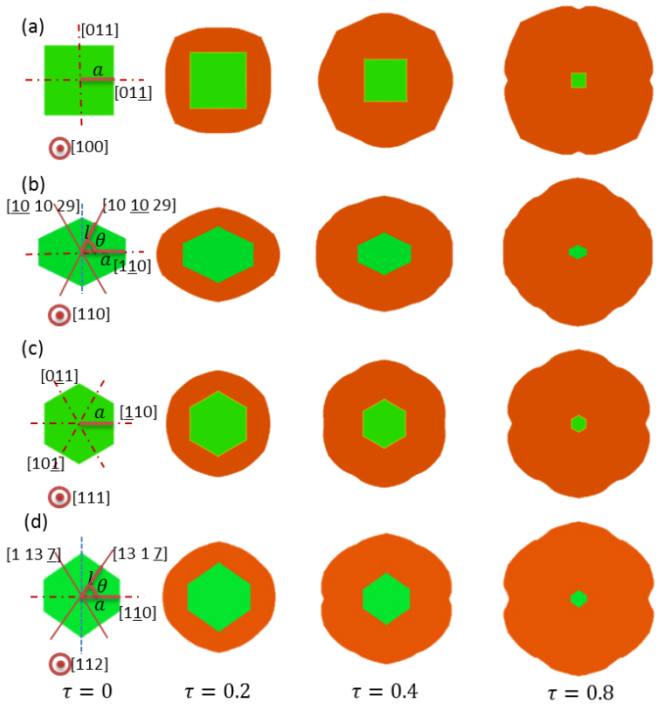

Figure S5. Lithiation simulation of c-Si pillars with designed polygonal cross section shapes. The original cross sections at τ=0 and snapshots of the morphology of a-Li_xSi shell (red) and c-Si core (green) at τ = 0.2, 0.4 and 0.8 are shown for (a) <100>, (b) <110>, (c) <111> and (d) <112> pillars.

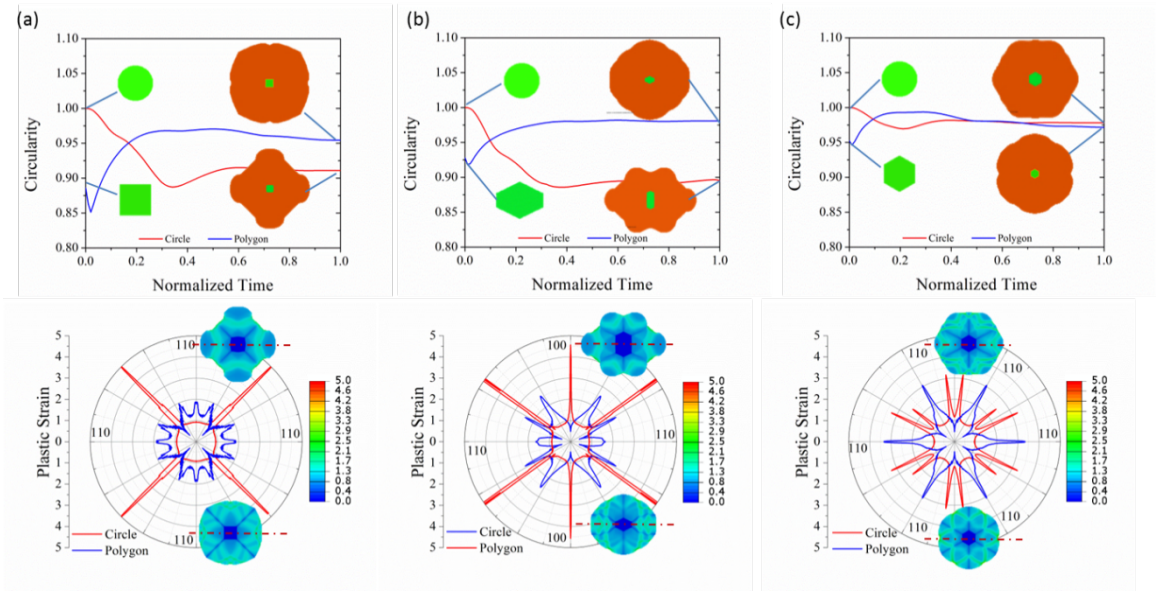

Figure S6. Comparison of the time evolution of the circularity (upper panel) and PEEQ distribution (at $\tau = 0.6$) within the cross section plane (lower panel) of circular (red curves) and polygonal pillars (blue curves) for (a) <100>, (b) <110> and (c) <111>-oriented pillars.

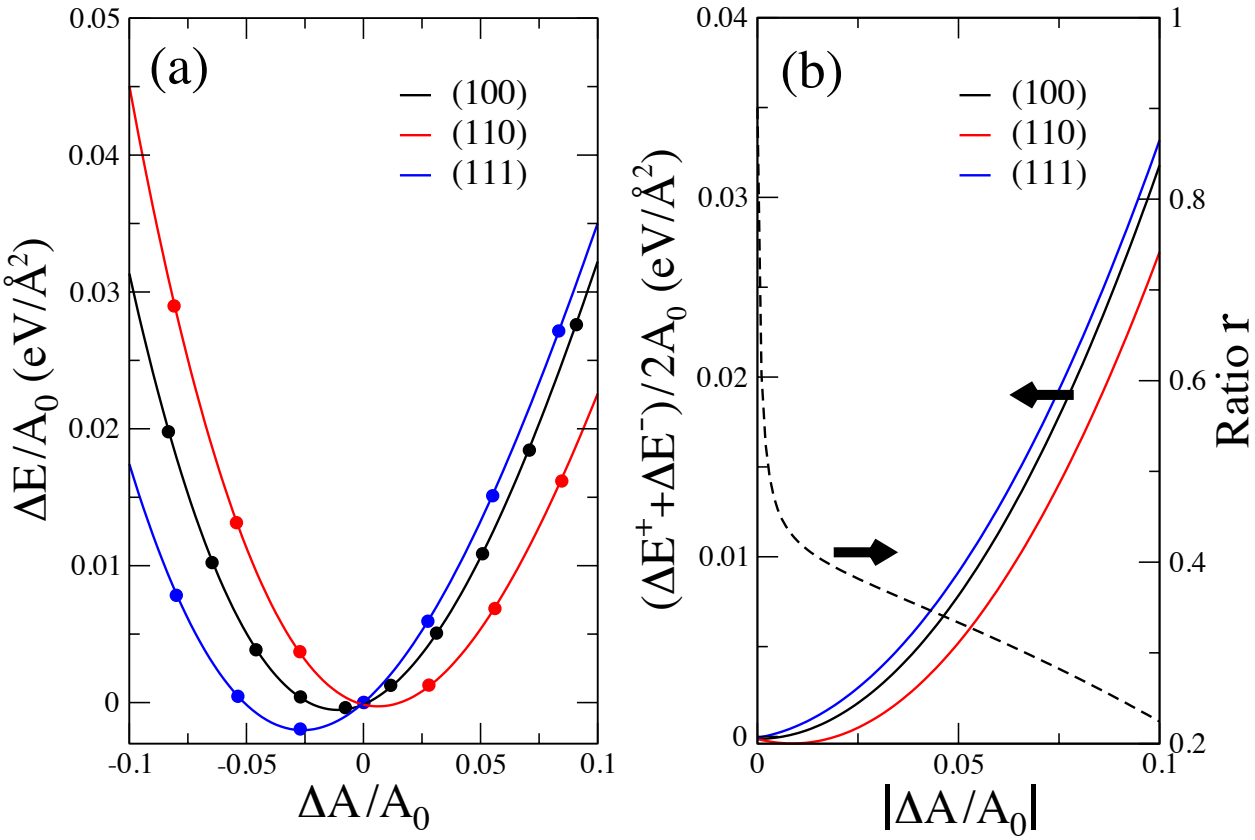

Figure S7. Procedure for estimating ordering of Li reaction front velocities based on strain induced in a Si surface slab upon lithiation, calculated by DFT. (a) Area-normalized strain energy $\Delta E / A_0$ for the (100), (110), and (111) surface slabs. Here, $\Delta A / A_0$ is the relative areal strain (negative/positive = compressive/tensile; the zero value represents the surface area at the equilibrium bulk lattice parameter), and ΔE is the associated change in total internal energy. (b) Left axis: Total area-normalized strain energy $s = \left(\Delta E^{+} + \Delta E^{-}\right) / 2A_0$ as a function of local strain magnitude $|\Delta A / A_0|$, obtained by averaging the surface slab strain energy under local compressive strain and under tensile strain. Here, ΔE^{+} and ΔE^{-} are changes in total internal energy associated with the application of tensile (+) and compressive (-) strain of the same magnitude. Right axis: Dependence of the ratio r on $|\Delta A / A_0|$.

References

1. An, Y.; Jiang, H. *Model Simul Mater Sc* **2013,** 21, (7), 074007.
2. Shao, Q.; Voss, L. F.; Conway, A. M.; Nikolic, R. J.; Dar, M. A.; Cheung, C. L. *Applied Physics Letters* **2013,** 102, (6), -.
3. Vanderbilt, D. *Phys Rev B* **1990,** 41, (11), 7892-7895.
4. Perdew, J. P.; Burke, K.; Ernzerhof, M. *Physical Review Letters* **1996,** 77, (18), 3865-3868.
5. Paolo, G.; Stefano, B.; Nicola, B.; Matteo, C.; Roberto, C.; Carlo, C.; Davide, C.; Guido, L. C.; Matteo, C.; Ismaila, D.; Andrea Dal, C.; Stefano de, G.; Stefano, F.; Guido, F.; Ralph, G.; Uwe, G.; Christos, G.; Anton, K.; Michele, L.; Layla, M.-S.; Nicola, M.; Francesco, M.; Riccardo, M.; Stefano, P.; Alfredo, P.; Lorenzo, P.; Carlo, S.; Sandro, S.; Gabriele, S.; Ari, P. S.; Alexander, S.; Paolo, U.; Renata, M. W. *Journal of Physics: Condensed Matter* **2009,** 21, (39), 395502.
6. Monkhorst, H. J.; Pack, J. D. *Phys Rev B* **1976,** 13, (12), 5188-5192.
7. Lee, S. W.; McDowell, M. T.; Choi, J. W.; Cui, Y. *Nano Letters* **2011,** 11, (7), 3034-3039.